Published online 18 November 2021

Nucleic Acids Research, 2021, Vol. 49, No. 21 ***12411–12421***
https://doi.org/10.1093/nar/gkab1072

Probing the stability of the SpCas9–DNA complex after cleavage

Pierre Aldag[1], Fabian Welzel[1], Leonhard Jakob[2], Andreas Schmidbauer[2], Marius Rutkauskas[1], Fergus Fettes[1], Dina Grohmann[2,3] and Ralf Seidel[1,*]

[1]Peter Debye Institute for Soft Matter Physics, University of Leipzig, Leipzig 04103, Germany, [2]Institute of Microbiology & Archaea Centre, Single-Molecule Biochemistry Lab, University of Regensburg, Regensburg 93053, Germany and [3]Regensburg Center of Biochemistry (RCB), University of Regensburg, 93053 Regensburg, Germany

Received August 04, 2021; Revised October 14, 2021; Editorial Decision October 15, 2021; Accepted October 20, 2021

ABSTRACT

CRISPR–Cas9 is a ribonucleoprotein complex that sequence-specifically binds and cleaves double-stranded DNA. Wildtype Cas9 and its nickase and cleavage-incompetent mutants have been used in various biological techniques due to their versatility and programmable specificity. Cas9 has been shown to bind very stably to DNA even after cleavage of the individual DNA strands, inhibiting further turnovers and considerably slowing down *in-vivo* repair processes. This poses an obstacle in genome editing applications. Here, we employed single-molecule magnetic tweezers to investigate the binding stability of different *Streptococcus pyogenes* Cas9 variants after cleavage by challenging them with supercoiling. We find that different release mechanisms occur depending on which DNA strand is cleaved. After initial target strand cleavage, supercoils are only removed after the collapse of the R-loop. We identified several states with different stabilities of the R-loop. Most importantly, we find that the post-cleavage state of Cas9 exhibits a higher stability than the pre-cleavage state. After non-target strand cleavage, supercoils are immediately but slowly released by swiveling of the non-target strand around Cas9 bound to the target strand. Consequently, Cas9 and its non-target strand nicking mutant stay stably bound to the DNA for many hours even at elevated torsional stress.

INTRODUCTION

CRISPR (Clustered Regularly Interspaced Short Palindromic Repeats)–Cas (CRISPR associated) systems constitute adaptive immune systems against nucleic acid-containing invaders in prokaryotic cells (1). CRISPR–Cas9 from the bacterial species *Streptococcus pyogenes* (SpCas9) is a 158 kDa protein that forms a ribonucleoprotein (RNP) complex with a CRISPR–RNA (crRNA) and a trans-activating RNA (tracrRNA). This complex can site-specifically target double-stranded DNA (dsDNA) and induces a double-strand break using its RuvC and HNH nuclease domains (2–4). Since its discovery, SpCas9 and other Cas9 variants have been widely used in rapidly emerging genome engineering applications in prokaryotic, plant and animal cells (5–7).

The target specificity of SpCas9 is mainly encoded by the 20 nt spacer region at the 5′ end of the crRNA. The tracrRNA and crRNA can be replaced by a single-guide RNA chimera (sgRNA) (4) which simplifies RNP formation. A prerequisite for site-specific DNA targeting is a three-nucleotide PAM sequence (protospacer-adjacent motif, NGG for SpCas9) next to the target site. SpCas9 weakly interacts with suitable PAM sites via facilitated diffusion (8). PAM recognition triggers an initial melting of the DNA double strand and primes base pairing between the crRNA spacer and the DNA target strand while displacing the non-target strand such that a so-called R-loop structure is formed (Figure 1A) (9). R-loop expansion is initiated from the PAM proximal nucleotides over the entire spacer region and constitutes the actual recognition of matching targets. In case of strongly mismatched targets, R-loop expansion is impeded and stops or the R-loop collapses (10). Successful base pairing between target strand and crRNA spacer is verified by two conformational changes of the SpCas9 RNP. Formation of an R-loop intermediate of 9 bp length triggers the transition into a 'checkpoint' state, opening up a channel to further accommodate the target strand–crRNA hybrid. This channel is formed upon a conformational change of the REC2 and REC3 domains (11,12). In this state, the HNH domain is still positioned >30 Å away from the cleavage site in the target strand. The second transition into the 'docked' state is induced once the R-loop reaches the PAM-distal end, causing a large movement of the HNH domain to reach its site of catalytic activity (13–15). The presence of magnesium ions as cofactor is a prerequisite for the

*To whom correspondence should be addressed. Tel: +49 341 9732501; Email: ralf.seidel@physik.uni-leipzig.de
Present address: Leonhard Jakob, Department of Pharmacology and Toxicology, Institute of Pharmacy, University of Regensburg, Regensburg 93053, Germany.

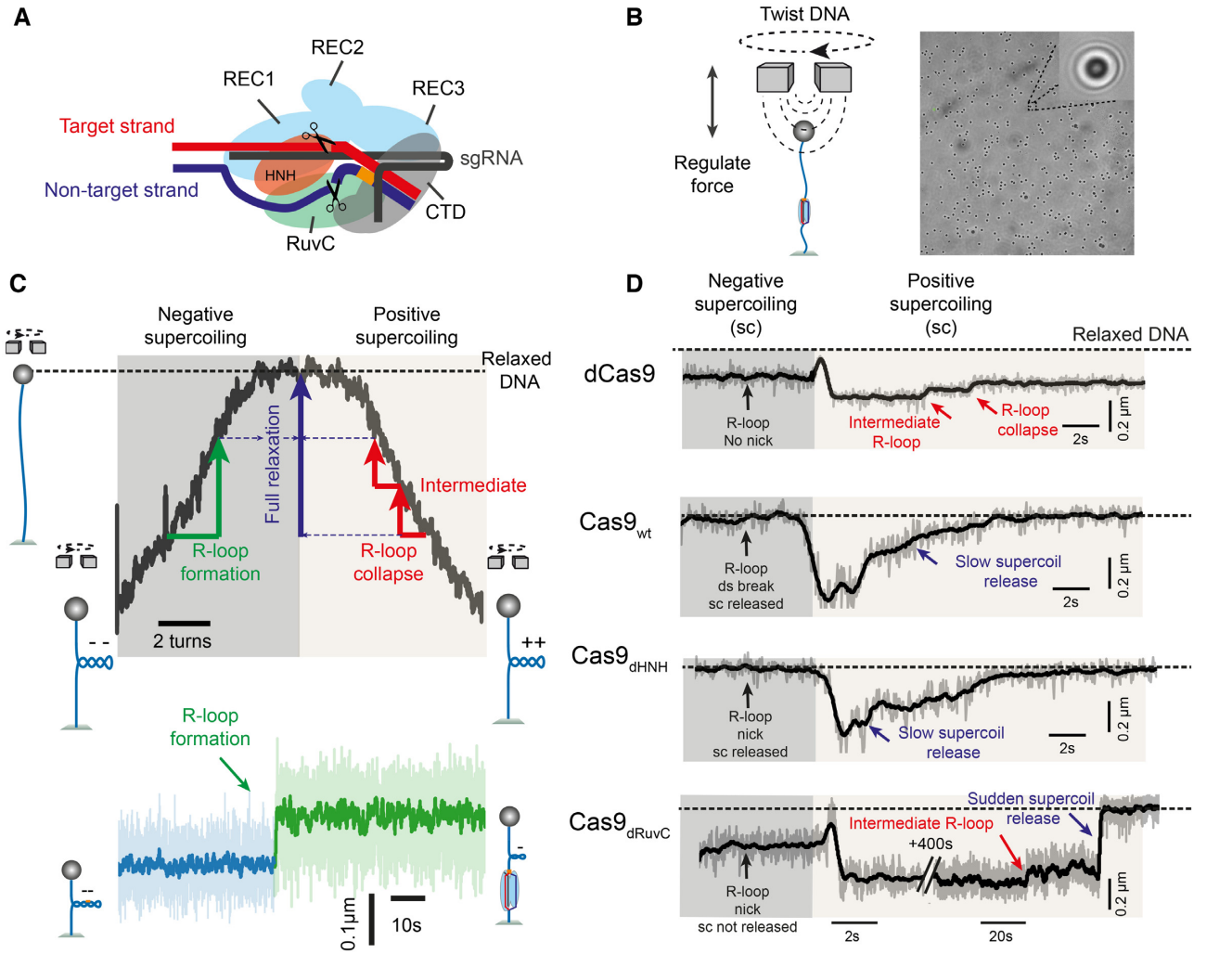

Figure 1. Experimental setup to measure the response of R-loops to supercoiling. (**A**) Schematic representation of the SpCas9–sgRNA ribonucleoprotein complex forming an R-loop on double-stranded DNA. The scissors indicate the active sites of the RuvC and HNH nuclease domains. The orange section on the non-target strand represents the PAM. (**B**) Schematic representation of the magnetic tweezers assay used to twist single double-stranded DNA molecules, which are tethered at either end to the surface of the fluidic cell and to a magnetic microbead. A pair of permanent magnets allows the application of a stretching force and molecule twisting. Up to one hundred beads were tracked in parallel (right: full microscope image with enlarged view of a single bead in the inset). (**C**) Top: Representative DNA supercoiling curve taken at 0.3 pN showing the characteristic DNA length reduction due to writhe formation upon twisting. Arrows depict the observed supercoil release for R-loop formation (green), the two-step R-loop collapse (red), and complete DNA relaxation (purple). Bottom: Representative time trajectory of the DNA length of a negatively supercoiled molecule (–6 turns, 0.3 pN), exhibiting a DNA length jump due to R-loop formation by $Cas9_{wt}$. (**D**) Representative time trajectories when challenging R-loops formed by dCas9, $Cas9_{wt}$, $Cas9_{dHNH}$ and $Cas9_{dRuvC}$ with positive supercoiling (sc). Trajectories were recorded at 120 Hz (light grey) and smoothed to 6 Hz (black). Arrows are colored corresponding to Figure 1C, top.

transition into the docked state. Furthermore, the transition is also inhibited when four or more PAM-distal mismatches are present. The target strand is cleaved first by the HNH domain, followed by cleavage of the non-target strand by the RuvC domain (16). After cleavage, SpCas9 undergoes an additional conformational change into a post-cleavage product state (12,17). In this state, the HNH domain undocks from the cleavage site and is thought to adopt a disordered state. After inducing a double-strand break, an extremely slow release of the DNA products essentially limits SpCas9 to undergo further turnovers (16,18). This results in an inhibited and slow *in vivo* DNA repair process (19,20). However, even for target bound SpCas9, the 3′ end of the cleaved non-target strand can be released and targeted by complementary ssDNA or 3′ to 5′ ssDNA exonucleases (17,20).

Introducing inactivating point mutations at positions D10A (RuvC) or H840A (HNH) turns SpCas9 into target strand or non-target strand nickases, respectively (4). Cas9 nickase mutants and cleavage-incompetent Cas9 (dCas9), which carries both mutations, have been used in various genome editing applications to increase specificity or to avoid double-strand breaks (21,22). Fusion of Cas9 variants with other enzymes, such as the repair enzyme Rad51, the endonuclease FokI, or an engineered reverse transcriptase, expanded the repertoire of Cas9-mediated DNA-targeting functionalities (22–24). While a large body of research has investigated the structure of the conformational states of

SpCas9 during R-loop formation and after DNA cleavage, the stability of the SpCas9–DNA complex in these states and their dependence on supercoiling remains elusive. Developing a thorough understanding of the post-cleavage stability of SpCas9 and the respective mutants can be helpful to improve the efficiencies of genome editing techniques.

Here, we investigated the post-cleavage state stability of SpCas9 and its respective nickase mutants by challenging it with supercoiling using single-molecule magnetic tweezers experiments (9,25,26). We show that SpCas9 bound to a target with a dsDNA break or a nicked non-target strand can easily relax superhelical tension. It can thus not be dissociated in processes that generate this kind of mechanical stress, such as transcription and replication (27–29). In contrast, SpCas9 bound to an intact target or a target with a nicked target strand cannot release superhelical tension and can thus be dissociated from the DNA when elevated tension is induced. In both cases, protein states with different stabilities are found, indicating dynamic structural transitions in the post-cleavage state. We show that dissociation from a target DNA with a nicked target strand requires considerably higher levels of supercoiling compared to an intact target, suggesting an increased stability of the post-cleavage conformational state.

MATERIALS AND METHODS

DNA substrates for magnetic tweezers measurements

Double-stranded DNA constructs for magnetic tweezers experiments with lengths of 1500 bp and 2700 bp were prepared as previously described (26). Briefly, a single copy of a given protospacer matching the spacer of the SpCas9 sgRNA and including a 5′-AGG-3′PAM on the non-target strand (see Supplementary Table S1) was cloned using the SmaI site of a pUC19 plasmid. From that plasmid, a 1.5 or 2.7 kb fragment including the SpCas9 target site was amplified by PCR, using primers in which either a NotI or a SpeI restriction enzyme site was introduced (see Supplementary Table S1). After digestion with NotI and SpeI, the fragment was ligated at either end to ∼600-bp-PCR fragments containing multiple biotin (SpeI site) or digoxigenin (NotI site) modifications (30).

sgRNA synthesis for magnetic tweezers experiments

The template for T7 transcription of the SpCas9 single sgRNA was generated by PCR, using the High Fidelity Phusion Polymerase (Thermo Fisher Scientific) and overlapping oligonucleotides. RNAs were produced by *in vitro* transcription using the TranscriptAid T7 High Yield Transcription Kit (Thermo Fisher Scientific) and purified using the GeneJet RNA Cleanup and Concentration Kit (Thermo Fisher Scientific). The sequences of the oligonucleotides and sgRNA used in this study are available in Supplementary Table S1.

Preparation of SpCas9

Plasmids for the expression of wildtype SpCas9 and the catalytically inactive SpCas9 variants carrying the mutations D10A/H840A were obtained from Addgene (plasmid ID: 39312 and 39318). SpCas9 variants that carried a single mutation of the catalytic site (D10A or H840A) were generated by site-directed mutagenesis using the wildtype SpCas9 expression plasmid as template. Expression was performed in *Escherichia coli* BL21 (DE3) cells. Expression and cell lysis conditions were chosen as described by Jinek *et al*. (4). The cleared cell lysate was applied to a HisTrap FF Ni-NTA affinity column (GE healthcare) equilibrated with HisA buffer (20 mM HEPES pH 7.5, 100 mM NaCl, 5 mM $MgCl_2$, 5% (v/v) glycerol, 20 mM imidazole). The column was washed with 2 column volumes (cv) of HisA buffer and 10 cv of HisA buffer containing 1 M NaCl to liberate unspecifically bound nucleic acids from SpCas9. Subsequently, the column was equilibrated with 2 cv of HisA buffer and pre-eluted with 2 cv buffer HisA with increased imidazole concentration of 40 mM. In the final elution step, the column was washed with 5 cv elution buffer (20 mM HEPES pH 7.5, 100 mM NaCl, 5 mM $MgCl_2$, 5% (v/v) glycerol, 200 mM imidazole). Elution fractions were pooled and digested with 50 U AcTEV protease (Thermo Fisher Scientific) over night at 4°C. The cleaved His6-MBP-tag was removed by gel filtration using a HiLoad 16/60 Superdex 200 column (GE healthcare) equilibrated in size exclusion buffer (20 mM Tris–HCl, 150 mM NaCl, 5 mM $MgCl_2$, 5% (v/v) glycerol, 1 mM DTT). Elution fractions contained nucleic acid free SpCas9 or SpCas9 variants ($A_{260/280} < 0.6$). Fractions were flash frozen in liquid nitrogen and stored at −80°C.

Reconstitution of guideRNA-SpCas9 complexes

For characterizing DNA cleavage, SpCas9 was pre-loaded with either a sgRNA or a pre-annealed crRNA:tracrRNA complex (Supplementary Tables S1 and S2). To reconstitute SpCas9-RNA complexes, a stock solution containing 1 μM SpCas9 and 1 μM guide RNA in 1x Cas buffer (20 mM Tris–HCl pH 7.5, 100 mM NaCl, 10 mM $MgCl_2$, 2% (v/v) glycerol, 1 mM DTT, 0.05% (v/v) Tween20) was incubated for 10 min at room temperature followed by a centrifugation step (20 000 g, 5 min, room temperature).

Plasmid–DNA cleavage assays

As substrate for plasmid-DNA cleavage assays, we cloned target plasmid (pM53.1; 6290 bp) containing the sequence of the *Saccharomyces cerevisiae* PHO5 gene with its native genomic context 500 bp upstream and downstream of the gene in a pBluescript vector backbone. The PHO5 locus was amplified from yeast genomic DNA using primers 5′-GGCCGCAGATCAAGTCAGAG-3′ and 5′-GCAAGTCACGAGAAATACCA-3′. The gene is flanked by a *Zygosaccharomyces rouxii* sequence-specific recombinase R recognition site (RS) upstream, and a triple *E. coli* LexA binding site downstream of the gene followed by another RS element. The plasmid was generated making use of pM49.2 containing the upstream RS element and the downstream triple LexA binding site and RS element (for details of the cloning procedure see (31)). Reconstituted SpCas9–sgRNA complexes were added in 10-fold excess to 5 nM pM53.1 plasmid DNA containing the target sequence and a 5′-AGG-3′ PAM motif in 1× Cas buffer. For

kinetic analysis, 15 μl samples were taken at different time points and the reactions were stopped by addition of EDTA (83 mM final concentration). Subsequently, SpCas9 was digested by the addition of 0.36 U Proteinase K (Thermo Fisher Scientific) followed by an incubation at 55°C for one hour. After Proteinase K digestion, 6x DNA loading dye (10 mM Tris–HCl pH 7.5, 0.03% bromophenol blue (w/v), 60% glycerol (v/v), 6 mM EDTA) was added to the samples and fragments were resolved on a 0.9% agarose gel. Cleavage products were visualized using a ChemiDoc Imaging System (Bio-Rad) after ethidium bromide staining of the agarose gel.

Magnetic tweezers experiments

The measurements were performed in a custom-built magnetic tweezers setup allowing the GPU-assisted real-time tracking of the DNA length for up to 100 DNA molecules in parallel (32). DNA constructs for the tweezers experiments were bound to magnetic beads of 1 μm-diameter (MyOne; Invitrogen) and flushed into the glass flowcell of the setup allowing the anchoring of the digoxigenin-modified end to the anti-digoxigenin coated surface of the cell (30,33). After removing unbound beads by flushing, force was applied by lowering the magnets towards the flow cell and DNA tethered beads were selected. Using bead tracking with a camera (Mikrotron EoSens), the length of the individual DNA molecules was determined and the applied forces were calibrated (34). During experiments, desired forces on the DNA construct could be set by placing the magnets at a particular distance from the flow cell according to the calibration results. Supercoiling of DNA was achieved by turning the magnets. The resulting torque that depended mainly on the stretching force was calculated based on previous theoretical work (35,36). Time trajectories of the DNA length were recorded at 120 Hz and smoothed with a sliding average to 6 Hz for analysis. For measurements with SpCas9, reconstituted SpCas9-sgRNA was added in tweezers buffer (20 mM Tris–HCl (pH 8.0), 100 mM NaCl, 10 mM $MgCl_2$ and 1 mg/ml BSA) at a concentration of 0.25 or 0.5 nM. For experiments with dCas9, the 1500 bp DNA construct was used because it allowed a high resolution for detection of the different R-loop states. For all other measurements, length changes were larger due to nicking of the DNA, such that the longer 2700 bp DNA construct was taken. After adding SpCas9, DNA length changes were monitored in real-time. For experiments where we exclusively challenged the DNA-bound SpCas9 complex, SpCas9 was allowed to prebind to negatively supercoiled DNA in the flowcell for 20 min to ensure efficient R-loop formation on most molecules before the experiment was started. The successful formation of an R-loop was confirmed by the occurrence of a pronounced change in DNA length.

Data analysis

Data analysis for the tweezers experiments was performed with Origin (OriginLab) and custom-built Matlab (The Mathworks Inc.) scripts.

Supercoil release velocities. For $Cas9_{dHNH}$ experiments, a slow supercoil release was observed. The velocities of the release were determined in Matlab by performing linear fits to the individual release events (see Figure 2). The velocities at each particular torque were then plotted in a histogram and fitted with a Gamma distribution. The Gamma distribution describes the total waiting time t of n successive events with exponentially distributed dwell times with mean value $1/\lambda$. The Gamma distribution is given by:

$$f\ (t) = \frac{e^{-\lambda t} \cdot \lambda^n \cdot t^{n-1}}{(n-1)!}\ .$$

By using this distribution, we assume that SpCas9 releases the non-target strand in one turn at a time, with each turn released after an exponentially distributed time with the same mean waiting time $1/\lambda$.

R-loop collapse times. To determine transition times, R-loop transitions into the intermediate state or full collapse were fitted by step functions in Matlab. Survival plots of the collapse times were then fitted with bi- or tri-exponential functions using Origin.

RESULTS

Multiplex magnetic tweezers measurements of the post-cleavage behavior of SpCas9

To investigate the post-cleavage behavior of different SpCas9 variants, we employed a single-molecule DNA twisting assay on a high-throughput magnetic tweezers platform (32). Numerous 2.7 kb dsDNA molecules containing a single SpCas9 target site matching the crRNA spacer and multiple biotin or digoxigenin modifications at either end were attached on the respective DNA end to 1 μm streptavidin-coated superparamagnetic beads and to the antidigoxigenin-coated surface of the flowcell of the setup. The three-dimensional positions of multiple DNA-tethered beads were tracked in parallel in a home-built microscope (37), allowing the real-time observation of the DNA length of the molecules (Figure 1B). The field gradient from a pair of magnets enabled the application of force onto the DNA molecule. The force could be controlled by adjusting the distance between the magnets and the flow cell. Turning the magnets allowed supercoiling of the DNA molecules in parallel. To monitor R-loop formation by SpCas9, we applied negative supercoiling, which reduces the DNA length due to writhe formation (Figure 1C, top). R-loop formation unwinds the DNA by about two turns, which absorbs a corresponding number of the applied supercoils such that it becomes visible as a sudden increase in the DNA length (Figure 1C, bottom).

As was previously shown for cleavage-incompetent dCas9 and other CRISPR–Cas effector complexes, the application of positive twist on DNA can promote the collapse of the R-loop and dissociation of the complex (9,10,26). In a simplified view, the R-loop is wrung out with the opposing superhelicity. To reproduce this, we added dCas9 into our flow cell and let it form R-loops on negatively supercoiled DNA. After R-loop formation, the DNA exhibited reduced but stable negative supercoiling since dCas9 left the DNA intact (Figure 1D, first trajectory, left). We then introduced positive supercoiling. R-loop collapse was now ob-

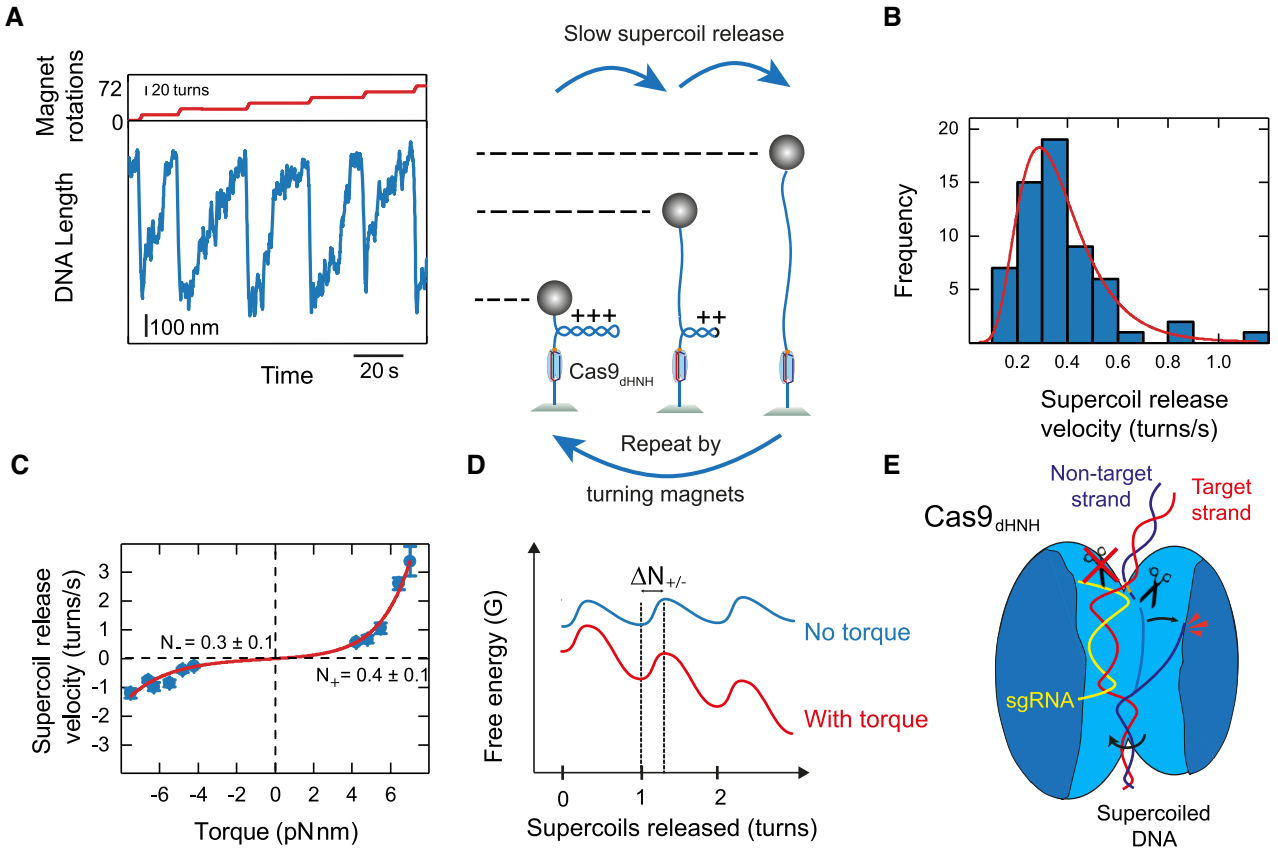

Figure 2. Velocity of supercoil release after non-target strand cleavage by $Cas9_{dHNH}$. (**A**) Representative time trajectories of repeated supercoil release after nicking and initial supercoil release has occurred. The trajectory was recorded at 120 Hz and smoothed to 6Hz (blue). Upon repeated step-wise DNA supercoiling ($\Gamma = +4.7$ pNnm, 12 turns), the DNA length was shortened. Supercoil release was detected as a slow increase in DNA length, which is limited by friction due to the presence of $Cas9_{dHNH}$. (**B**) Histogram of the measured supercoil release velocities given in turns per second (blue bars, $N = 60$) at negative supercoiling ($\Gamma = -4.7$ pN nm). The individual release velocities were obtained on a single DNA molecule. The red line shows a fit with a Gamma distribution. (**C**) Torque-dependence of the supercoil release velocity (blue). The error-bars correspond to the standard error of the mean. The red line shows a fit of the data with Equation (1). (**D**) Hypothetic scheme of the energy landscape for non-target strand release. The energy landscape is tilted downhill if positive or negative torque is applied (red line) in contrast to the absence of torque (blue line). (**E**) Cartoon illustrating the supercoil release for DNA nicked by $Cas9_{dHNH}$. When the non-target strand of a supercoiled dsDNA is cleaved, the applied torque is released by swivelling of the non-target strand around the target strand. The swivelling is sterically obstructed by the protein.

servable as a sudden DNA length change that occured in two steps (Figure 1D, first trajectory, right). The first step corresponded to the transition into the checkpoint state, i.e. to an R-loop shortening to the partial R-loop state (10). The second step corresponded to the final collapse of the partial R-loop and, typically, the dissociation of the protein. The resulting stable positive supercoiling indicated that the DNA remained intact.

We started to test the stability of the post-cleavage product state by challenging R-loops formed by wildtype SpCas9 ($Cas9_{wt}$ thereafter), SpCas9 with a mutated HNH domain ($Cas9_{dHNH}$ thereafter), and SpCas9 with a mutated RuvC domain ($Cas9_{dRuvC}$ thereafter) with positive supercoiling. The activities and cleavage kinetics of the individual enzymes were confirmed in a bulk cleavage assay (Supplementary Figure S1). In the case of nicking of any of the two strands, one would expect the supercoiling to be rapidly released, such that the DNA would reach the full length of the relaxed state (see supercoiling curve in Figure 1C at zero turns). Since nicking leads to the loss of torsional constraint, an additional supercoiling of the nicked DNA should no longer be possible (38). Cutting of the second strand would result in a double-strand break and loss of the magnetic bead.

When adding $Cas9_{wt}$ into the flow cell with negatively supercoiled DNA, the DNA tethers in the magnetic tweezers stayed in place for several hours (Supplementary Figure S2), even though the enzyme induced double-strand breaks (DSBs) within ~2 min after enzyme addition in bulk (Supplementary Figure S1). This indicated that $Cas9_{wt}$ remained stably bound to both DNA ends as previously reported (13,17,18). However, the molecule length corresponded to relaxed DNA (Figure 1D, second trajectory, left), as would be expected for nicked DNA, due to a loss of supercoiling shortly after R-loop formation (Supplementary Figure S2). Surprisingly, despite the presence of a potential nick, positive (and negative) supercoils could still be introduced (Figure 1D, second trajectory, right). However, the introduced supercoiling was not stable. Instead, an immediately starting but slow release of all applied supercoils was ob-

served (Figure 1D, second trajectory, Supplementary Figure S3). After release, additional supercoils could be repeatedly introduced (Supplementary Figure S3). This behavior resembled that of eukaryotic topoisomerase IB, which nicks DNA and releases twist by a free swivel mechanism in which the release velocity is reduced by protein friction (39). The slow supercoil release, which was consistently observed, supported the idea that $Cas9_{wt}$ remained bound to its target site holding the DNA ends together to prevent rupture of the tether.

$Cas9_{dHNH}$, which solely nicks the non-target strand of the DNA, showed a similar behavior as $Cas9_{wt}$. The negatively supercoiled DNA relaxed after R-loop formation (Figure 1D, third trajectory, left) and additional supercoils could be introduced, which then slowly relaxed (Figure 1D, third trajectory, right, Supplementary Figure S4). This indicated, also for $Cas9_{dHNH}$, a swivel mechanism in which stably bound $Cas9_{dHNH}$ slowed down the release of supercoiling. Since for $Cas9_{dHNH}$ only the non-target strand is nicked, the swivel must occur around the intact target strand with the externally bound non-target strand end(s) detaching from Cas9 during supercoil release.

In contrast, for $Cas9_{dRuvC}$, which induces a nick on the target strand within less than a minute (Supplementary Figure S1), negatively supercoiled DNA molecules did not become relaxed after R-loop formation for extended periods of time (Figure 1D, fourth trajectory, left, Supplementary Figure S5). Furthermore, we did not observe an immediately starting supercoil release at positive supercoiling. Instead, the supercoiling level remained constant for prolonged times (Figure 1D, fourth trajectory, middle). This was not unexpected, since the nicked target strand in $Cas9_{dRuvC}$ remains hybridized to the sgRNA. Supercoil release via this nick would require collapse of the R-loop structure and most likely dissociation of the RNP. In agreement with this idea, applied positive supercoiling was finally completely released in a fast, sudden step (Figure 1D, fourth trajectory, Supplementary Figure S6). Such fast supercoil release is indicative of a DNA nick in absence of bound protein (38), suggesting that $Cas9_{dRuvC}$ dissociated from the DNA upon R-loop collapse, leaving a free nick behind. This was further supported by the observation that the fast release of all supercoils was frequently preceeded by a short substep indicative of the first step of R-loop collapse seen for dCas9 (see small step in Figure 1D, first trajectory). Note that we attribute the fast DNA relaxation only to spontaneous R-loop collapse and assume that target strand cleavage has already occurred before, since the incubation time of 20 minutes at negative supercoiling in our experiments is much longer than the cleavage time of the target strand observed in bulk cleavage experiments (Supplementary Figure S1).

Bound $Cas9_{dHNH}$ releases supercoiling in a swivel-like manner

Next, we investigated the different responses of the SpCas9 variants to supercoiling after DNA cleavage in more detail. $Cas9_{wt}$ and $Cas9_{dHNH}$ released positive and negative supercoiling slowly by a swivel mechanism (Figure 2A, Supplementary Figure S4). For this, a cleaved non-target strand appeared to be the pre-requisite. Since $Cas9_{wt}$ cleaves first the target strand followed by the cleavage of the non-target strand (16), we conclude that $Cas9_{wt}$ has already introduced a dsDNA break when releasing supercoils by swiveling. During this process, the DNA ends are thus held together by the target strand, which is hybridized to the sgRNA, in agreement with previous findings (40).

For $Cas9_{dHNH}$, we carefully characterized the supercoil release velocity as function of the applied positive and negative supercoiling levels. For both supercoiling directions, a similar release behavior was recorded (Supplementary Figure S4A). Application of different forces allowed to vary the acting torque during supercoil release (see Materials and Methods). We measured the velocity of individual release events by applying a linear fit through each event (Supplementary Figure S4B). At each respective torque, we determined the linear slopes of the supercoiling curve, which allowed us to convert the velocity from nanometers per second to turns per second. The distributions of the release velocities had a pronounced maximum and were well described by a Gamma distribution (Figure 2B). The Gamma distribution describes a process containing n discrete substeps, each with an exponentially distributed dwell time (see Materials and Methods). For the parameter, which describes the number of substeps in the process, we obtained, on average, $n = 6.6 \pm 1.3$ and $n = 4.3 \pm 0.3$ for positive and negative supercoiling, respectively. These numbers agreed well with the number of turns within the linear regime of the supercoiling curve indicating that the release of supercoils occurs in discrete successive steps of one turn at a time. The mean release velocities approximately showed an exponential increase with the applied torque for positive and negative supercoiling (Figure 2C). Following Arrhenius transition-state rate theory, we modeled the supercoil release as a step-wise process in which supercoils can be released (or introduced) as single full turns. For this process, a periodic energy landscape can be drawn with energy minima at full turns (corresponding to the non-target strand docked onto $Cas9_{dHNH}$) and transition state maxima in between (corresponding to a detached non-target strand and partially turned DNA) (Figure 2D). Applied torque tilts the energy landscape to favor supercoil release. The torque dependence can be described using an exponential Arrhenius-term in which the activation energy required to reach the transition state is changed by the work to reach the transition state in presence of the torque. To consider supercoil release in positive and negative direction and to ensure a zero net release at zero torque, two torque-dependent Arrhenius-terms were used:

$$v\ (\Gamma) = v_0 \cdot \left(\exp\left(\frac{\Gamma \cdot 2\pi \cdot \Delta N_+}{k_b T} \right) - \exp\left(-\frac{\Gamma \cdot 2\pi \cdot \Delta N_-}{k_b T} \right) \right), \quad (1)$$

where v_0 is the spontaneous swiveling rate in either direction at zero torque, Γ is the applied torque, and $\Delta N_{+/-}$ are the angular distances of the transition state from the energy minima for positive and negative supercoil release, respectively. Fitting this model to the data in Figure 2C yielded transition state distances of $\Delta N_+ = 0.4 \pm 0.1$ turns and $\Delta N_- = 0.3 \pm 0.1$, indicating that the transition state is located approximately half a turn from the energy minima. The swiveling rate at zero torque was $v_0 = 0.04 \pm 0.01$ turns/s. Thus, $Cas9_{dHNH}$ spontaneously introduces or depletes a single supercoil every ~25 s even for relaxed DNA.

Overall, this data supports a model in which $Cas9_{dHNH}$ releases the non-target strand by a swiveling mechanism

governed by torque and friction (Figure 2E). Due to the slight difference in the transition state distance, the release occurred slightly faster at positive than negative torque.

Target strand cleavage causes two differently stable SpCas9 states

In a next step, we explored the stability of $Cas9_{dRuvC}$ in the post-cleavage state on DNA when subjected to supercoiling. $Cas9_{dRuvC}$ only cleaves the target strand, such that supercoils cannot be released by non-target strand detachment and swiveling around the protein (Figure 3A). Rather, at positive supercoiling, R-loop collapse is observed with the familiar intermediate step, followed by full supercoil release in a sudden rapid step similar to the free nick generated by a nicking enzyme (Figure 3B, Supplementary Figure S6) (38). Supercoil release was not seen at negative supercoiling, since negative supercoiling stabilizes the R-loop and prevents its collapse. After R-loop collapse, repeated introduction of additional supercoiling failed for several minutes, providing further evidence that the enzyme dissociated upon R-loop collapse (Figure 3C). After that waiting time, the introduction of supercoils became possible again, indicating that a new $Cas9_{dRuvC}$ molecule had bound to the nicked target site.

We carefully investigated the stability of $Cas9_{dRuvC}$ bound to the target site after nicking. To this end, we incubated the protein and DNA in the flowcell at negative supercoiling to allow R-loop formation. We then induced positive twist on the DNA to enforce the collapse of the R-loop, and characterized the time between introduction of positive supercoiling and the collapse of the full R-loop. The dwell times of the intermediate state were comparably small with respect to the stability of the complex (Supplementary Figure S7). The R-loop collapse times were best described by a bi-exponential distribution (Figure 3D). Therefore, we propose the existence of two distinct states, distinguishable by their collapse times on the order of minutes for the unstable state and hours for the stable state. Repeating the experiment at different applied torques, we observed an exponential dependence of the R-loop collapse time on the torque for both states (Figure 3E). This indicated the presence of a transition state for R-loop collapse (similar to the supercoil release above) as observed previously for various CRISPR–Cas proteins (9,10,26,41). Fitting the torque dependent data with a single Arrhenius function provided angular distances to the transition states of 0.18 ± 0.03 turns and 0.07 ± 0.01 turns for the unstable and stable state, respectively. This corresponds to a DNA rewinding (most likely at the PAM-distal end) of about 2 and 1 bp. Furthermore, the fitting allowed to extrapolate the collapse times to zero torque for which we obtained 408 ± 58 min and 3.2 ± 1.5 min for the stable and the unstable state, respectively. On average, $72 \pm 3\%$ of the R-loops were in the stable state and $28\% \pm 3\%$ in the unstable state with no obvious torque-dependence (Figure 3F). We did not observe any dsDNA release by $Cas9_{wt}$ until many hours after cleavage. This suggests that the occurrence of the unstable state after target strand cleavage is unique to $Cas9_{dRuvC}$ and does not occur in case of $Cas9_{wt}$, since stable target strand capturing would only be possible for a formed R-loop.

Overall, the results support that $Cas9_{dRuvC}$ stays tightly bound to the target after target strand cleavage until the full R-loop collapses. During this time, the $Cas9_{dRuvC}$–sgRNA–DNA complex can adopt different conformational states, possibly in a dynamic manner.

The post-cleavage product state stabilizes the R-loop in a torque-dependent manner

To reveal the relative stability of the post-cleavage state, we finally investigated the stability of SpCas9 in the pre-cleavage state. To this end, we challenged intact R-loops formed by a catalytically fully inactive dCas9 variant with positive supercoiling (Figure 4A). The measurements were performed in presence of magnesium, allowing dCas9 to adopt the 'docked' conformation of the HNH domain. As described before, R-loops formed by dCas9 collapsed in two steps at positive torque (Figure 4B). The first step can be attributed to the transition from the docked to the intermediate state as observed for $Cas9_{dRuvC}$. The second step, which was limited only to partial supercoiling release due to the lack of a DNA nick, can be attributed to the collapse of the intermediate state and dissociation of dCas9. Allowing a new R-loop formation at negative turns, the collapse process could be repeated multiple times (Supplementary Figure S8). The R-loop collapse times were best described by an exponential distribution with three distinct components, therafter called stable, semi-stable, and unstable state (Figure 4C, Supplementary Figure S9). As for $Cas9_{dRuvC}$, R-loop collapse occurred in two distinct steps for all three components. The respective collapse times fell into the range of hours, minutes, and seconds with each component showing a slight torque dependence (Figure 4D). Compared to $Cas9_{dRuvC}$, the collapse time for the stable state was slightly decreased, while the collapse time of the unstable state did not significantly change. The occurrence of a torque-dependent semi-stable state was not observed for $Cas9_{dRuvC}$. This may indicate flexibility of the docked state of dCas9. Similar to $Cas9_{dRuvC}$, the fraction of molecules in the unstable state did not change with torque (Figure 4E). However, the fraction of molecules in the semi-stable state increased, while the fraction of molecules in the stable state decreased with increasing torque. Due to the torque dependence of the fraction of molecules found in the different populations, the mean time of the R-loop collapse was strongly dependent on the torque applied (Figure 4F). When comparing these results to $Cas9_{dRuvC}$ (Figure 4F), we found that the mean time of the R-loop collapse was generally higher for $Cas9_{dRuvC}$ compared to dCas9. This indicates a further stabilization of SpCas9 after target strand cleavage. The stabilization was found to be torque-dependent with pronounced stabilization at high torques. To correlate the two states with different stabilities to known conformations of SpCas9, we carried out experiments in absence of Mg^{2+} at which the docked state of SpCas9 is suppressed (14). Even though the docked state was suppressed, a full R-loop was formed (Supplementary Figure S10A). We obtained an average collapse time that matched the collapse time of the previously observed unstable state (Supplementary Figure S10B). This suggests that the stable and semi-stable states represent the docked conformation of SpCas9.

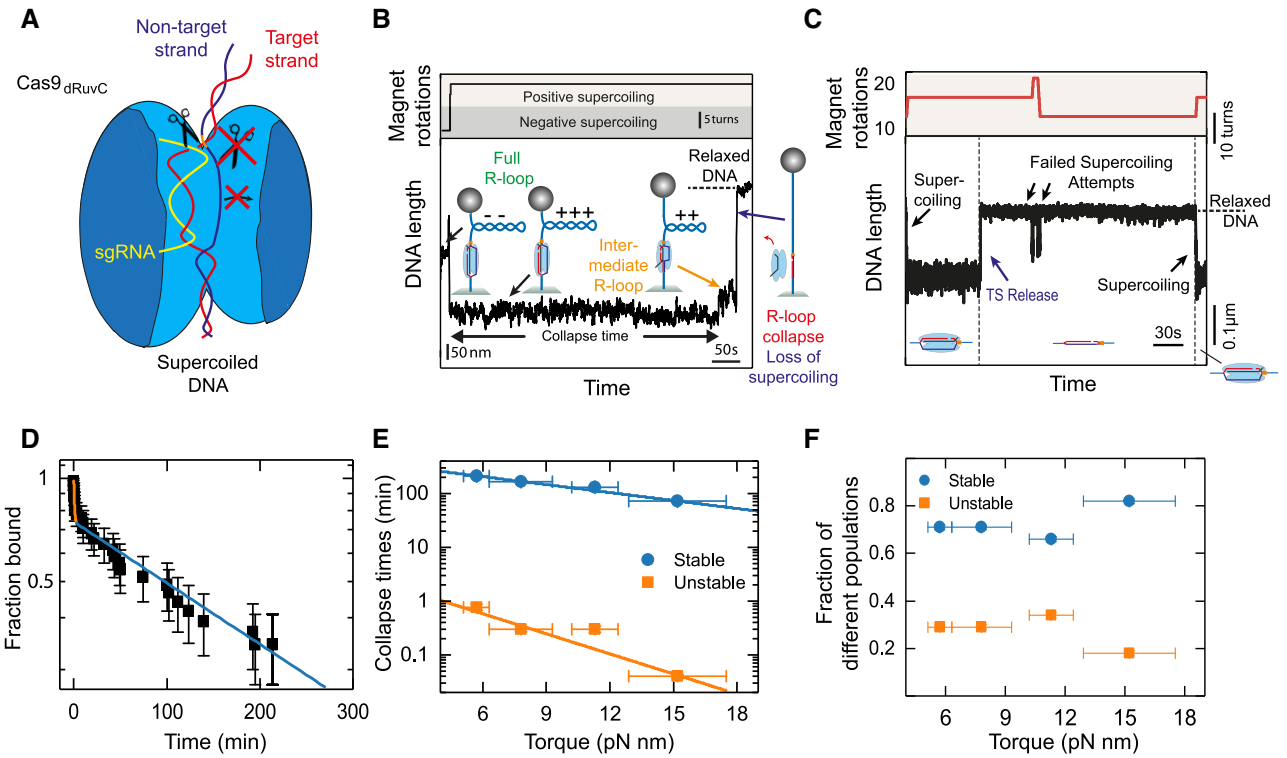

Figure 3. Stability of the $Cas9_{dRuvC}$–crRNA–DNA complex after target strand cleavage. (**A**) Cartoon illustrating the nicking of the target strand by $Cas9_{dRuvC}$. The target strand is nicked but remains tightly bound to $Cas9_{dRuvC}$ such that supercoils are not released in presence of the protein. (**B**) Representative magnetic tweezers trajectory (smoothed to 6 Hz) showing data for an experiment in which $Cas9_{dRuvC}$ nicked the DNA and the complex is challenged by strong positive supercoiling (high positive torque). No supercoils are released until part of the R-loop collapses (see orange arrow). This is followed by a rapid release of all supercoiling as observed for nicked DNA in absence of protein (red arrow). (**C**) Characteristic magnetic tweezers trajectory of DNA length after nicking with $Cas9_{dRuvC}$ (smoothed to 6 Hz). An R-loop is preformed. Positive supercoiling is induced while $Cas9_{dRuvC}$ is bound to the target. After some time, the R-loop collapses and the supercoiling is lost due to the nick in the target strand. Subsequently, the nick in the DNA prevents further supercoiling until, supposedly, another Cas9 forms a new R-loop after several minutes and the DNA regains its supercoilability. In this example, the transient intermediate sub-step during R-loop collapse is too short to be visible at this scale. (**D**) Survival plot of the introduced R-loops (black squares) fitted with a bi-exponential decay function (orange/blue line). Errors correspond to binomial errors with $\sigma = \sqrt{p \cdot (1-p)/N}$. The data was taken from an experiment with 37 individual DNA molecules tracked in parallel. (**E**) Characteristic time constants for the R-loop collapse as function of torque obtained from the bi-exponential fits revealing an unstable (orange) and a stable (blue) population of R-loops. Errors on collapse times correspond to the standard error of the mean. Errors on torque correspond to standard errors of the mean from the different beads. (**F**) Torque-dependence of the fractions of unstable (orange) and stable (blue) R-loops.

Note that the obtained collapse times were longer than for recently reported measurements with *S. thermophilus* Cas9, for which no intermediate step was observed (42).

In conclusion, we showed that dCas9 adopts three different conformations when a full R-loop has been formed. Additionally, we observed a torque-dependent stabilization of the R-loop after cleavage of the target strand.

DISCUSSION

Several studies showed that SpCas9 stays tightly bound to its target DNA after cleavage of double-stranded DNA is completed. In this study, we elucidate the mechanisms by which SpCas9 achieves this high stability even under unfavorable conditions of positive supercoiling, a situation encountered during transcription and replication of genomic DNA. Using single-molecule magnetic tweezers measurements, we show that the post-cleavage behavior of SpCas9 strongly depends on which strand of the target site is cleaved.

We could show that non-target strand cleavage allows the non-target strand to detach from the protein and to swivel around the target strand under friction. By this mechanism, even high supercoiling levels are quickly relaxed such that R-loop collapse and SpCas9 dissociation are circumvented. We determined a spontaneous swivel rate of 0.04 ± 0.01 turns/s at zero torque. This provides evidence for a spontaneous release of the non-target strand even in absence of supercoiling such that it becomes accessible for complementary ssDNA or exonucleases (17).

A different behavior was observed for the $Cas9_{dRuvC}$ variant, which can only cleave the target strand. Here, a supercoil release in presence of the enzyme was impeded. As observed in the cryo-EM structure of the post-cleavage state of SpCas9 (12), the cleaved target strand stays hybridized to the sgRNA. Thus, supercoil release could only occur by collapse of the whole R-loop structure, requiring elevated positive torque. R-loop collapse was associated with subsequent dissociation of $Cas9_{dRuvC}$.

By carefully analyzing the collapse times, we observed two states of different stabilities with collapse times in the order of a few minutes and several hours, respectively. After target strand cleavage, the HNH domain has been reported to be highly flexible (12,17). The different stability

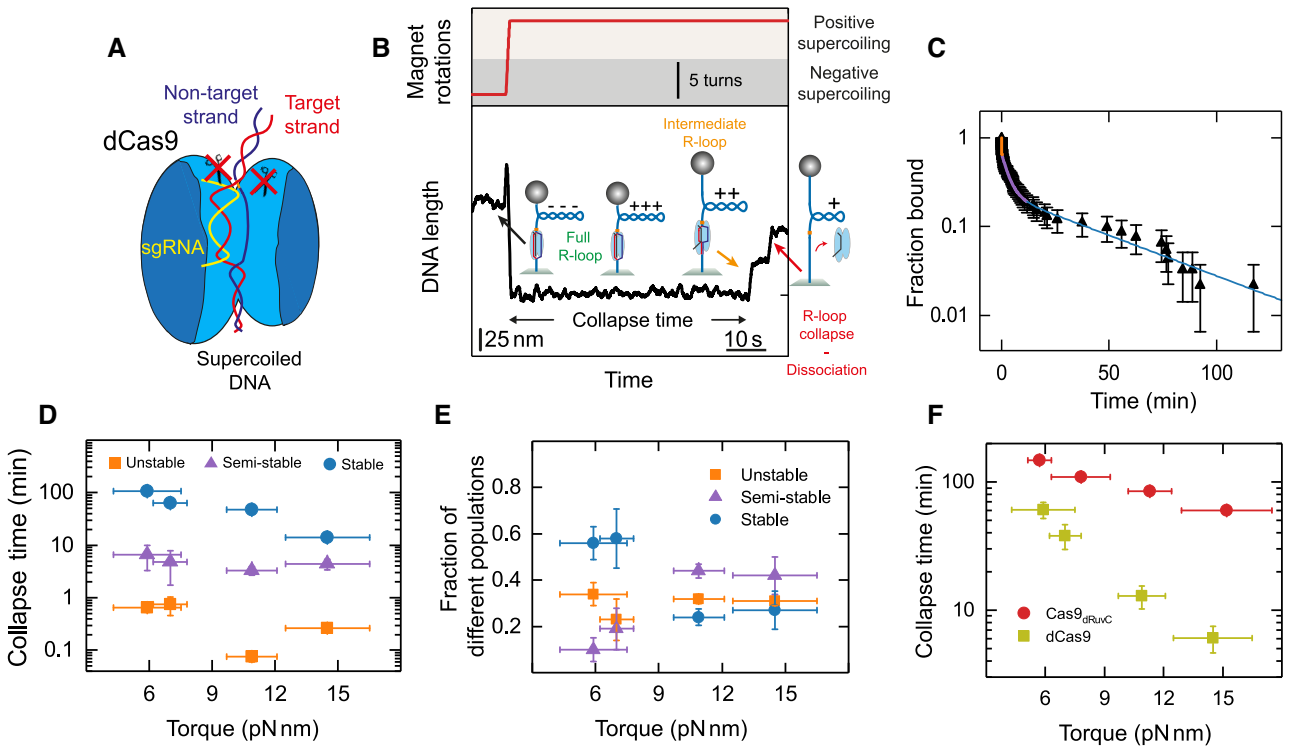

Figure 4. Stability of the dCas9-crRNA-dsDNA complex. (**A**) Cartoon illustrating the pre-cleavage state of SpCas9, a state produced by the cleavage-incompetent dCas9 variant. (**B**) Representative magnetic tweezers trajectory (smoothed to 6 Hz) when challenging an R-loop formed by dCas9 with positive supercoiling. The R-loop spontaneously collapses in two characteristic steps. Absence of full supercoil release indicates that the DNA was not nicked by dCas9. (**C**) Survival plot of R-loops formed by dCas9 (black triangles) fitted with a tri-exponential decay function (orange/purple/blue line). Errors correspond to binomial errors with $\sigma = \sqrt{p \cdot (1-p)/N}$. The data was recorded with 92 DNA molecules tracked in parallel. (**D**) Characteristic time constants for the R-loop collapse as function of torque obtained from the tri-exponential fits revealing an unstable (orange), a semi-stable (purple), and a stable (blue) population of R-loops. (**E**) Torque-dependence of the fractions of unstable (orange), semi-stable (purple), and stable (blue) R-loops. Errors on collapse times correspond to the standard error of the mean. Errors on torque correspond to standard errors of the mean from the different beads. (**F**) Mean R-loop collapse time averaged over all populations for dCas9 (green) and $Cas9_{dRuvC}$ (red). Cleavage of the target strand appears to stabilize SpCas9 on the DNA. The errors correspond to the standard of the mean.

states observed in this work might stem from this flexibility. There has been some debate on the dynamics of the pre-cleavage conformational states. While some studies have shown that SpCas9 reaches a stable, cleavage-competent 'docked' conformation in the presence of Mg^{2+} ions (14,43), other studies have observed only short excursions into the docked state with the majority of time spent in the 'checkpoint' conformation (15,44,45). Our results suggest that even though a complete R-loop is formed and cleavage is carried out, $Cas9_{dRuvC}$ exhibits conformational flexibility, transitioning between an undocked state and a stabilized post-cleavage state. It is possible that the assigned undocked state corresponds to the previously reported conformational 'checkpoint' state. However, in support of our assignment, we note that for the corresponding unstable R-loop events, a full R-loop is formed as confirmed by the presence of the intermediate step during R-loop collapse. For wildtype SpCas9, we did not observe DNA release after cleavage of both DNA strands even after several hours of measurement, indicating that, in contrast to $Cas9_{dRuvC}$, it does not enter the undocked state with low stability after cleavage.

Cleavage-incompetent dCas9 exhibits even three distinct states and, potentially, a higher conformational flexibility. Combining the results of $Cas9_{dRuvC}$ and dCas9 we suggest that the stable state, which is observed for both variants, corresponds to the post-cleavage product state. This state appears to be transiently visited even for the uncleaved target, albeit only at low levels of supercoiling. The semi-stable state is observed when dCas9 is bound to the target DNA without DNA cleavage. This state dominates under conditions of high supercoiling and most likely corresponds to the pre-cleavage state with a docked HNH domain. The unstable state is found for both dCas9 and $Cas9_{dRuvC}$ and most likely represents the undocked state in agreement with the previously observed dynamic sampling between the different states (Figure 5) (15,44,45).

For $Cas9_{wt}$, both DNA strands are cut and it tightly 'holds on' to the two DNA ends, in agreement with previous reports (18,40). This tight clamping should be mainly achieved by the crRNA–target strand hybrid since detachment and swiveling of the non-target strand did not promote $Cas9_{wt}$ dissociation. This can neatly explain the strong strand bias when RNA polymerase dislodges Cas9 from dsDNA breaks (46). Cas9 displacement is only successful when RNA polymerase destroys the R-loop upon transcribing the target strand. In contrast, transcription and detachment of the non-target strand has little effect on Cas9 binding since positive supercoils generated by the RNA polymerase are readily released.

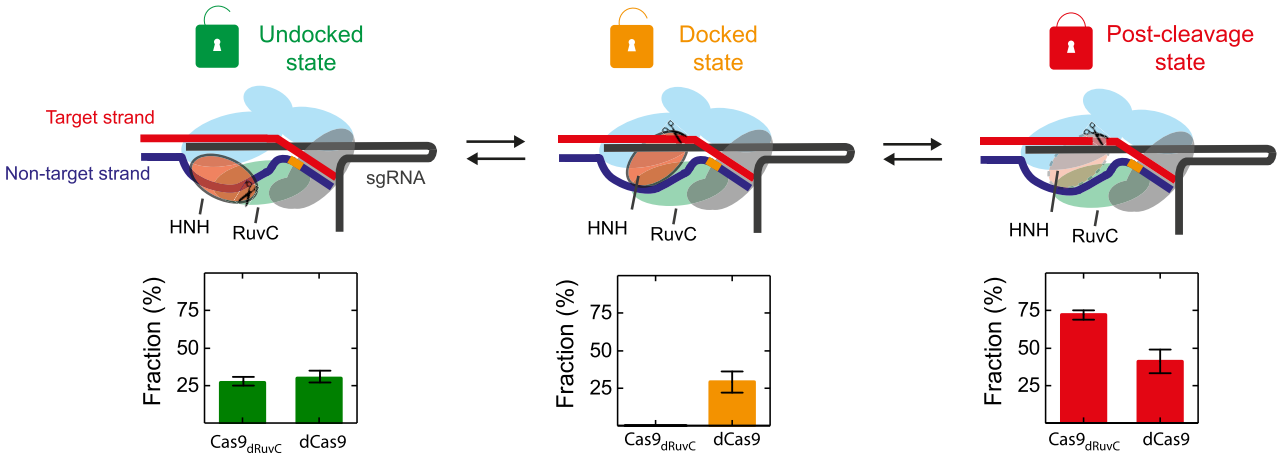

Figure 5. Scheme of the different states of SpCas9 on intact and nicked DNA targets. We assigned the unstable state to a full R-loop with undocked HNH domain, the semi-stable state to the pre-cleavage state with the HNH domain docked to the active site, and the stable state to the post-cleavage product state with a disordered (or flexible) HNH domain (12,17). Catalytically inactive dCas9 can occupy all states and most likely samples these states in a dynamic manner. $Cas9_{dRuvC}$ was predominantly found in the stable (post-cleavage) state and rarely occupied the unstable state.

Overall, the dominance of the post-cleavage product state accompanying target strand cleavage stabilizes the R-loop compared to the uncut target, especially at higher torques. This suggests that, under *in-vivo* conditions, SpCas9 has evolved to remain bound to its cut target in agreement with the observation that the dissociation time of SpCas9 is as long as the generation time in bacterial cells (47). Possibly, this not only inactivates the invader DNA but may generally slow down transcription and/or replication of the foreign DNA. Notably, a post-cleavage stabilization of the R-loop and the trapping of supercoiling has recently been observed for the Type V-A CRISPR–Cas effector complex Cas12a (48). Contrarily, a Cas9 variant from *Staphylococcus aureus* has been observed to be a multiple turnover enzyme indicating that diverse strategies may be used to impede foreign DNA invasion by regulating the post-cleavage behavior of the effector complexes (49).

Overall, the presented results expand the knowledge about the post-cleavage state(s) of SpCas9 and the mechanisms by which SpCas9 avoids R-loop collapse and dissociation even under high twist that can be generated *in vivo* by the genome processing machineries (28). Generally, the high stability of SpCas9 on DNA after cleavage represents a challenge for efficient genome engineering applications. Nickase mutants of Cas9 have been used in various approaches for genome editing with strong differences in results depending on which nickase was used (23,50,51). Our findings may help to understand the described differences and might facilitate future genome editing applications with SpCas9 nickases.

SUPPLEMENTARY DATA

Supplementary Data are available at NAR Online.

ACKNOWLEDGEMENTS

We thank Joachim Griesenbeck for providing the pM53.1 plasmid. Furthermore, we thank Virginijus Siksnys, Tautvydas Karvelis, and Greta Bigelytė for providing the sgRNA.

FUNDING

Deutsche Forschungsgemeinschaft [SPP2141 to R.S. and D.G.]; European Research Council [GA 724863 to R.S.]. Funding for open access charge: Deutsche Forschungsgemeinschaft [SPP2141] and Leipzig University.
Conflict of interest statement. None declared.

REFERENCES

1. Barrangou,R., Fremaux,C., Deveau,H., Richards,M., Boyaval,P., Moineau,S., Romero,D.A. and Horvath,P. (2007) CRISPR provides acquired resistance against viruses in prokaryotes. *Science (New York, N.Y.)*, **315**, 1709–1712.
2. Garneau,J.E., Dupuis,M.-È., Villion,M., Romero,D.A., Barrangou,R., Boyaval,P., Fremaux,C., Horvath,P., Magadán,A.H. and Moineau,S. (2010) The CRISPR/Cas bacterial immune system cleaves bacteriophage and plasmid DNA. *Nature*, **468**, 67–71.
3. Gasiunas,G., Barrangou,R., Horvath,P. and Siksnys,V. (2012) Cas9-crRNA ribonucleoprotein complex mediates specific DNA cleavage for adaptive immunity in bacteria. *Proc. Natl. Acad. Sci. U.S.A.*, **109**, E2579–E2586.
4. Jinek,M., Chylinski,K., Fonfara,I., Hauer,M., Doudna,J.A. and Charpentier,E. (2012) A programmable dual-RNA-guided DNA endonuclease in adaptive bacterial immunity. *Science (New York, N.Y.)*, **337**, 816–821.
5. Cong,Le, Ran,F.A., Cox,D., Lin,S., Barretto,R., Habib,N., Hsu,P.D., Wu,X., Jiang,W., Marraffini,L.A. *et al.* (2013) Multiplex genome engineering using CRISPR/Cas systems. *Science (New York, N.Y.)*, **339**, 819–823.
6. Mali,P., Yang,L., Esvelt,K.M., Aach,J., Guell,M., DiCarlo,J.E., Norville,J.E. and Church,G.M. (2013) RNA-guided human genome engineering via Cas9. *Science (New York, N.Y.)*, **339**, 823–826.
7. Hsu,P.D., Lander,E.S. and Zhang,F. (2014) Development and applications of CRISPR–Cas9 for genome engineering. *Cell*, **157**, 1262–1278.
8. Globyte,V., Lee,S.H., Bae,T., Kim,J.-S. and Joo,C. (2019) CRISPR/Cas9 searches for a protospacer adjacent motif by lateral diffusion. *EMBO J.*, **38**, e99466.
9. Szczelkun,M.D., Tikhomirova,M.S., Sinkunas,T., Gasiunas,G., Karvelis,T., Pschera,P., Siksnys,V. and Seidel,R. (2014) Direct observation of R-loop formation by single RNA-guided Cas9 and Cascade effector complexes. *Proc. Natl. Acad. Sci. U.S.A.*, **111**, 9798–9803.
10. Ivanov,I.E., Wright,A.V., Cofsky,J.C., Aris,K.D.P., Doudna,J.A. and Bryant,Z. (2020) Cas9 interrogates DNA in discrete steps modulated

by mismatches and supercoiling. *Proc. Natl. Acad. Sci. U.S.A.*, **117**, 5853–5860.
11. Jiang,F., Taylor,D.W., Chen,J.S., Kornfeld,J.E., Zhou,K., Thompson,A.J., Nogales,E. and Doudna,J.A. (2016) Structures of a CRISPR–Cas9 R-loop complex primed for DNA cleavage. *Science (New York, N.Y.)*, **351**, 867–871.
12. Zhu,X., Clarke,R., Puppala,A.K., Chittori,S., Merk,A., Merrill,B.J., Simonović,M. and Subramaniam,S. (2019) Cryo-EM structures reveal coordinated domain motions that govern DNA cleavage by Cas9. *Nat. Struct. Mol. Biol.*, **26**, 679–685.
13. Sternberg,S.H., LaFrance,B., Kaplan,M. and Doudna,J.A. (2015) Conformational control of DNA target cleavage by CRISPR–Cas9. *Nature*, **527**, 110–113.
14. Dagdas,Y.S., Chen,J.S., Sternberg,S.H., Doudna,J.A. and Yildiz,A. (2017) A conformational checkpoint between DNA binding and cleavage by CRISPR–Cas9. *Sci. Adv.*, **3**, eaao0027.
15. Yang,M., Peng,S., Sun,R., Lin,J., Wang,N. and Chen,C. (2018) The conformational dynamics of Cas9 governing DNA cleavage are revealed by single-molecule FRET. *Cell Rep.*, **22**, 372–382.
16. Raper,A.T., Stephenson,A.A. and Suo,Z. (2018) Functional insights revealed by the kinetic mechanism of CRISPR/Cas9. *J. Am. Chem. Soc.*, **140**, 2971–2984.
17. Wang,Y., Mallon,J., Wang,H., Singh,D., Hyun Jo,M., Hua,B., Bailey,S. and Ha,T. (2021) Real-time observation of Cas9 postcatalytic domain motions. *Proc. Natl. Acad. Sci. U.S.A.*, **118**, e2010650118.
18. Sternberg,S.H., Redding,S., Jinek,M., Greene,E.C. and Doudna,J.A. (2014) DNA interrogation by the CRISPR RNA-guided endonuclease Cas9. *Nature*, **507**, 62–67.
19. Brinkman,E.K., Chen,T., Haas,M., Holland,H.A., Akhtar,W. and van Steensel,B. (2018) Kinetics and fidelity of the repair of Cas9-induced double-strand DNA breaks. *Mol. Cell*, **70**, 801–813.
20. Richardson,C.D., Ray,G.J., DeWitt,M.A., Curie,G.L. and Corn,J.E. (2016) Enhancing homology-directed genome editing by catalytically active and inactive CRISPR–Cas9 using asymmetric donor DNA. *Nat. Biotechnol.*, **34**, 339–344.
21. Ran,F.A., Hsu,P.D., Lin,C.-Y., Gootenberg,J.S., Konermann,S., Trevino,A.E., Scott,D.A., Inoue,A., Matoba,S., Zhang,Y. *et al.* (2013) Double nicking by RNA-guided CRISPR Cas9 for enhanced genome editing specificity. *Cell*, **154**, 1380–1389.
22. Anzalone,A.V., Randolph,P.B., Davis,J.R., Sousa,A.A., Koblan,L.W., Levy,J.M., Chen,P.J., Wilson,C., Newby,G.A., Raguram,A. *et al.* (2019) Search-and-replace genome editing without double-strand breaks or donor DNA. *Nature*, **576**, 149–157.
23. Rees,H.A., Yeh,W.-H. and Liu,D.R. (2019) Development of hRad51-Cas9 nickase fusions that mediate HDR without double-stranded breaks. *Nat. Commun.*, **10**, 2212.
24. Guilinger,J.P., Thompson,D.B. and Liu,D.R. (2014) Fusion of catalytically inactive Cas9 to FokI nuclease improves the specificity of genome modification. *Nat. Biotechnol.*, **32**, 577–582.
25. Brutzer,H., Luzzietti,N., Klaue,D. and Seidel,R. (2010) Energetics at the DNA supercoiling transition. *Biophys J.*, **98**, 1267–1276.
26. Rutkauskas,M., Sinkunas,T., Songailiene,I., Tikhomirova,M.S., Siksnys,V. and Seidel,R. (2015) Directional R-loop formation by the CRISPR–Cas surveillance complex cascade provides efficient off-target site rejection. *Cell Reports*, **10**, 1534–1543.
27. Kouzine,F., Sanford,S., Elisha-Feil,Z. and Levens,D. (2008) The functional response of upstream DNA to dynamic supercoiling in vivo. *Nat. Struct. Mol. Biol.*, **15**, 146–154.
28. Ma,J., Bai,L. and Wang,M.D. (2013) Transcription under torsion. *Science (New York, N.Y.)*, **340**, 1580–1583.
29. Wu,H.-Y., Shyy,S., Wang,J.C. and Liu,L.F. (1988) Transcription generates positively and negatively supercoiled domains in the template. *Cell*, **53**, 433–440.
30. Luzzietti,N., Knappe,S., Richter,I. and Seidel,R. (2012) Nicking enzyme-based internal labeling of DNA at multiple loci. *Nat. Protocols*, **7**, 643–653.
31. Griesenbeck,J., Boeger,H., Strattan,J. and Kornberg,R.D. (2003) Purification of defined chromosomal domains. In: *Methods in Enzymology : Chromatin and Chromatin Remodeling Enzymes, Part A*. Academic Press, pp. 170–178.
32. Huhle,A., Klaue,D., Brutzer,H., Daldrop,P., Joo,S., Otto,O., Keyser,U.F. and Seidel,R. (2015) Camera-based three-dimensional real-time particle tracking at kHz rates and Ångström accuracy. *Nat. Commun.*, **6**, 5885.
33. Schwarz,F.W., Tóth,J., van Aelst,K., Cui,G., Clausing,S., Szczelkun,M.D. and Seidel,R. (2013) The helicase-like domains of type III restriction enzymes trigger long-range diffusion along DNA. *Science (New York, N.Y.)*, **340**, 353–356.
34. Daldrop,P., Brutzer,H., Huhle,A., Kauert,D.J. and Seidel,R. (2015) Extending the range for force calibration in magnetic tweezers. *Biophys J.*, **108**, 2550–2561.
35. Maffeo,C., Schöpflin,R., Brutzer,H., Stehr,R., Aksimentiev,A., Wedemann,G. and Seidel,R. (2010) DNA-DNA interactions in tight supercoils are described by a small effective charge density. *Phys. Rev. Lett.*, **105**, 158101.
36. Schöpflin,R., Brutzer,H., Müller,O., Seidel,R. and Wedemann,G. (2012) Probing the elasticity of DNA on short length scales by modeling supercoiling under tension. *Biophys J.*, **103**, 323–330.
37. Klaue,D. and Seidel,R. (2009) Torsional stiffness of single superparamagnetic microspheres in an external magnetic field. *Phys. Rev. Lett.*, **102**, 28302.
38. Crut,A., Koster,D.A., Seidel,R., Wiggins,C.H. and Dekker,N.H. (2007) Fast dynamics of supercoiled DNA revealed by single-molecule experiments. *Proc. Natl. Acad. Sci. U.S.A.*, **104**, 11957–11962.
39. Koster,D.A., Croquette,V., Dekker,C., Shuman,S. and Dekker,N.H. (2005) Friction and torque govern the relaxation of DNA supercoils by eukaryotic topoisomerase IB. *Nature*, **434**, 671–674.
40. Newton,M.D., Taylor,B.J., Driessen,R.P.C., Roos,L., Cvetesic,N., Allyjaun,S., Lenhard,B., Cuomo,M.E. and Rueda,D.S. (2019) DNA stretching induces Cas9 off-target activity. *Nat. Struct. Mol. Biol.*, **26**, 185–192.
41. Singh,D., Wang,Y., Mallon,J., Yang,O., Fei,J., Poddar,A., Ceylan,D., Bailey,S. and Ha,T. (2018) Mechanisms of improved specificity of engineered Cas9s revealed by single-molecule FRET analysis. *Nat. Struct. Mol. Biol.*, **25**, 347–354.
42. Mullally,G., van Aelst,K., Naqvi,M.M., Diffin,F.M., Karvelis,T., Gasiunas,G., Siksnys,V. and Szczelkun,M.D. (2020) 5′ modifications to CRISPR–Cas9 gRNA can change the dynamics and size of R-loops and inhibit DNA cleavage. *Nucleic Acids Res.*, **48**, 6811–6823.
43. Chen,J.S., Dagdas,Y.S., Kleinstiver,B.P., Welch,M.M., Sousa,A.A., Harrington,L.B., Sternberg,S.H., Joung,J.K., Yildiz,A. and Doudna,J.A. (2017) Enhanced proofreading governs CRISPR–Cas9 targeting accuracy. *Nature*, **550**, 407–410.
44. Osuka,S., Isomura,K., Kajimoto,S., Komori,T., Nishimasu,H., Shima,T., Nureki,O. and Uemura,S. (2018) Real-time observation of flexible domain movements in CRISPR–Cas9. *EMBO J.*, **37**, e96941.
45. Shibata,M., Nishimasu,H., Kodera,N., Hirano,S., Ando,T., Uchihashi,T. and Nureki,O. (2017) Real-space and real-time dynamics of CRISPR–Cas9 visualized by high-speed atomic force microscopy. *Nat. Commun.*, **8**, 1430.
46. Clarke,R., Heler,R., MacDougall,M.S., Yeo,N.C., Chavez,A., Regan,M., Hanakahi,L., Church,G.M., Marraffini,L.A. and Merrill,B.J. (2018) Enhanced bacterial immunity and mammalian genome editing via RNA-polymerase-mediated dislodging of Cas9 from double-strand DNA breaks. *Mole. Cell*, **71**, 42–55.
47. Jones,D.L., Leroy,P., Unoson,C., Fange,D., Ćurić,V., Lawson,M.J. and Elf,J. (2017) Kinetics of dCas9 target search in Escherichia coli. *Science*, **357**, 1420–1424.
48. Naqvi,M.M., Lee,L., Torres Montaguth,O.E. and Szczelkun,M.D. (2021) A gate and clamp regulate sequential DNA strand cleavage by CRISPR–Cas12a. bioRxiv doi: https://doi.org/10.1101/2021.06.18.448962, 18 June 2021, preprint: not peer reviewed.
49. Yourik,P., Fuchs,R.T., Mabuchi,M., Curcuru,J.L. and Robb,G.B. (2019) Staphylococcus aureus Cas9 is a multiple-turnover enzyme. *RNA*, **25**, 35–44.
50. Shen,B., Zhang,W., Zhang,J., Zhou,J., Wang,J., Chen,L., Wang,L., Hodgkins,A., Iyer,V., Huang,X. *et al.* (2014) Efficient genome modification by CRISPR–Cas9 nickase with minimal off-target effects. *Nat. Methods*, **11**, 399–402.
51. Miyaoka,Y., Berman,J.R., Cooper,S.B., Mayerl,S.J., Chan,A.H., Zhang,B., Karlin-Neumann,G.A. and Conklin,B.R. (2016) Systematic quantification of HDR and NHEJ reveals effects of locus, nuclease, and cell type on genome-editing. *Scientific Rep.*, **6**, 23549.